IEEE Access
Multidisciplinary ⋮ Rapid Review ⋮ Open Access Journal

Received April 5, 2022, accepted April 21, 2022, date of publication April 29, 2022, date of current version May 6, 2022.

Digital Object Identifier 10.1109/ACCESS.2022.3171337

Numerical and Experimental Study on Vertical Takeoff and Separation of the Compound Aircraft

DONG WANG[1,2], QIZHEN HONG[2,3], XIN HUANG[1,2], XINBIAO PEI[1], AND JING WANG[1]

[1]Changchun Institute of Optics, Fine Mechanics and Physics, Chinese Academy of Sciences, Key Laboratory of Space-Based Dynamic & Rapid Optical Imaging Technology, Chinese Academy of Sciences, Changchun 130033, China
[2]University of Chinese Academy of Sciences, Beijing 100049, China
[3]State Key Laboratory of High Temperature Gas Dynamics, Institute of Mechanics, Chinese Academy of Sciences, Beijing 100190, China

Corresponding author: Jing Wang (1551793853@qq.com)

The work was funded by the Science and Technology Development Plan Project of Jilin Province [No.202021294JC].

ABSTRACT The traditional technical solution to achieve vertical take-off of the fixed-wing aircraft is adding power components, which will inevitably increase the weight of the aircraft. This paper proposes a compound flight scheme to achieve vertical take-off for the fixed-wing aircraft, using the carrier aircraft with vertical take-off capability to carry the target aircraft. Compared with the vertical take-off performance of a single aircraft, the present scheme enables the target aircraft to have a larger carrying capacity and longer flight distance. In order to verify the feasibility of the current scheme, this paper first investigates the steady aerodynamic performance of the compound aircraft and the dynamical separation process by computational fluid dynamics simulation. The steady lift coefficient of the compound aircraft during the acceleration stage and the unsteady aerodynamic force during the separation stage are obtained and analyzed. Next, an unmanned aerial vehicle (with vertical take-off and horizontal acceleration capabilities) is designed specifically, and the flight experiments of the vertical take-off and separation processes are conducted. Successful separations are achieved many times in the flight tests, which validate the feasibility of the present scheme.

INDEX TERMS Compound aircraft, CFD, vertical take-off, dynamical separation of two aircraft.

I. INTRODUCTION

The vertical and/or short take-off and landing (V/STOL) aircraft have been extensively studied for a long time. Back in 1957, the Hawker P1127 was developed, and it used the vectored-thrust engine created by the Bristol Engine Company [1]. The project, later on, led to the well-known Hawker Harrier aircraft. Many types of V/STOL aircraft have been invented in the second half of the last century, to name just a few, Yak-38, MV-22 Osprey, NASA Puffin, and Lockheed XFV-1 [2]. The most notable success is the Lockheed Martin's X-35 demonstrator aircraft, whose performance on vertical short-term take-off and landing was tested successfully [3], and the armed version (named F-35 Lightning II) entered production in the early 21st century. Above successful practices prove the soundness of using the combination of lift engine and cruise engine on the fixed-wing aircraft to achieve V/STOL. However, the additional weight of the lift engine has a significant impact on the aircraft's flight performance. Comparing the F35B (with V/STOL capability) to the F35A (without V/STOL capability), the addition of power fans and other components increases the empty weight of the F35B by 1360.8 kg, and the flight distance is reduced by 523 km since the fuel volume is reduced by 2153 kg.[1] Therefore, how to possess the ability of V/STOL without degenerating its flight performance is an urgent issue to address.

The composite flight solution, i.e., using one fixed-wing aircraft to carry another or more fixed-wing aircraft, adds performance not available for a single aircraft. A new concept called Multifunctional Compound Aircraft [4], [5] was proposed by combining two or more aircraft and using their features each other to achieve a specific flight goal. Works have been devoted to developing the

The associate editor coordinating the review of this manuscript and approving it for publication was Halil Ersin Soken.

[1]https://www.f35.com/about

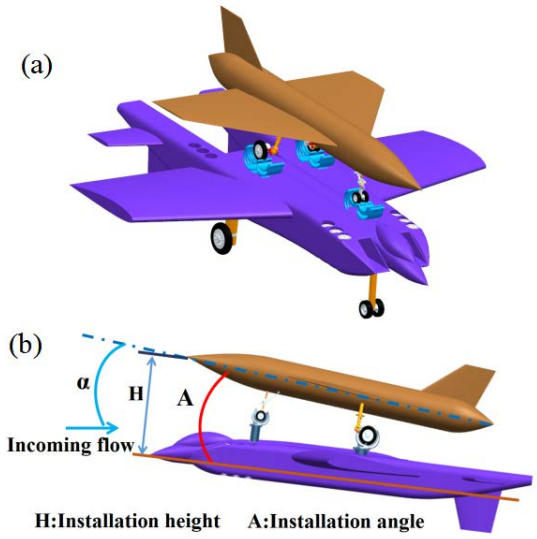

FIGURE 1. Schematic diagram of the compound aircraft. The upper aircraft is the target aircraft, and the lower one is the carrier aircraft.

compound aircraft, roughly divided into two categories, i.e., horizontal compound aircraft and vertical compound aircraft. A horizontal compound scheme connecting two aircraft wingtip-to-wingtip has been proposed and tested in the Tip-Tow project [6]. The wingtip-docked configuration showed aerodynamic benefits (around 20-40%) on the lift force [4], [6].

Besides horizontal compound aircraft, the proposal of vertical compound aircraft has also been studied [5], [7]–[9]. A reusable horizontal take-off/horizontal landing (HTHL) two-stage-to-orbit vertical compound aircraft has been designed to reduce the launch costs, and it brings payloads into low-earth orbit safely and economically [7]. The feasibility of the above concept was tested through a high-fidelity simulation. Ref. [8] used a twin-fuselage UAV as carrier aircraft to launch an orbiting vehicle, which shows that the launch cost of orbiting vehicle is greatly reduced due to reusability.

Moreover, a classical application using vertical compound transport is that a Boeing 747 was modified as a Shuttle Carrier Aircraft (SCA) to carry Space Shuttle Enterprise to altitude for the captive and free-flight tests [10]. The primary purpose is to use the power of the SCA to provide Enterprise with the height and speed needed for testing. The used connecting mechanism with integrated pressure sensors [11], which provides load measurement for the lift of the Space Shuttle to ensure the successful separation, is a good engineering reference for developing the connecting mechanism of vertical compound aircraft.

With the aim to make the aircraft possess the capabilities of long-distance flight, vertical take-off, and more considerable load weight, a new flight scheme is proposed in this paper. Specifically, as seen in Fig. 1, the new scheme leverages the concept of compound aircraft by using one aircraft to carry another aircraft, in which the lower one (called the carrier aircraft) adopts a combined power configuration of multiple lift engines and cruise engines. The merit of the present scheme is that the target aircraft have a better carrying capacity because it does not need to add a power system to achieve vertical take-off and landing. As mentioned before, the addition of power fans and other components increases the empty weight of the F35B (compared to F35A) by 1360 kg, and the flight distance and weapon load are reduced by 523 km and 1360 kg, respectively. Moreover, the target aircraft does not consume fuel during the vertical take-off process.

However, there are many technical problems in the concept of compound aircraft and the safe separation of two aircraft. The flow field of the compound aircraft becomes complicated due to the coupling of two aircraft. Furthermore, the separation is a dynamic process in which unsteady aerodynamic interference will occur. The unsteady aerodynamic interference results from the fact that the wings of the target aircraft and the carrier aircraft are aerodynamically coupled. The aerodynamic parameters of aircraft in a compound state are different from those flying as a single aircraft. The aerodynamic interaction between two wings in a parallel flight was investigated in Ref. [12]. The change of the tip-to-tip distance of the two aircraft would vary the aerodynamic center of lift [12], thus the rolling, pitching, and yawing moments are significantly affected. Moreover, the interaction between two foils was studied experimentally in Ref. [13], which presented measurements of the turbulent flow around a two-airfoil T-tail type arrangement and the aerodynamic coefficients. The variation of the tail lift coefficient with respect to the angle of attack, between a two-airfoil arrangement and a single airfoil, was also discussed [13]. The unsteady viscous flow fields of dual flapping airfoils in tandem configurations were simulated numerically in Ref. [14], in which aerodynamic interactions were studied, including flapping fore airfoil with fixed aft airfoil, two airfoils flapping in-phase and out-of-phase. The results indicated that the aft airfoil in the wake of the flapping fore airfoil has a significant influence on the aerodynamic performance.

Previous works have also been devoted to studying the dynamical separation between the carrier aircraft and the space rocket [15], store separation [16], [17], and separation dynamics of air-to-air missiles [18]. The above cases separate the rocket or missile downward. However, the separation process occurring in the present study is that the target aircraft separates upward, which is more complicated and different from the above cases in the literature. The theoretical and experimental study related to this problem is still scarce in the literature. Therefore, the aerodynamic performance during the separation stage will first be investigated numerically in this paper. Then the flight tests are conducted to investigate the realistic separation process.

The paper is organized as follows: Section 2 introduces a new scheme for vertical take-off employing the compound aircraft and reports the relative numerical simulation;

Section 3 gives details on the design of the carrier aircraft; Section 4 provides details about the aerodynamic study and flight tests of the compound aircraft; Section 5 reports the actual separation processes in the flight tests; Concluding remarks are given in the last section.

II. CONCEPTUAL DESIGN OF A NEW SCHEME FOR VERTICAL TAKE-OFF

A. THE COMPOUND AIRCRAFT SYSTEM

The new vertical take-off system consists of two aircraft, as already shown in Fig. 1. The carrier aircraft (in the lower position) carries the target aircraft (in the upper position) to achieve vertical take-off, then the target aircraft separates and performs its flight task. In the present vertical compound scheme, the carrier and target aircraft are designed as fixed-wing aircraft. Therefore, the present scheme enables most fixed-wing aircraft (as the target aircraft) to have the ability of vertical take-off. The fixed-wing carrier aircraft should add a set of locking mechanism on the back to connect with the landing gear tires of the target aircraft, and the locking mechanism unlocks the target aircraft when receiving the command of separation.

The power system of the carrier aircraft should provide enough lift for the vertical take-off of the two aircraft and sufficient horizontal thrust to reach a higher flight speed for separation. Thus, in addition to the conventional thrust engine, 12 lift engines (see Fig. 1 (a), the holes in the carrier aircraft are remained for installing the lift engines) are designed to serve as the lift source during the vertical take-off stage. Although the type selection and parameters of lift engines and thrust engine will not be reported in this paper, the aerodynamics performances of present aircraft configurations (see Fig. 1) are investigated in the following.

The aircraft were designed and optimized through Computational Fluid Dynamics (CFD) simulation. After several rounds of optimizations, the basic layout of the optimized carrier aircraft has double fuselages, trapezoidal upper single wings, flat tails, and lower double vertical tails. The lift distribution of the trapezoidal wing is close to the elliptical distribution, which reduces induced drag and increases the lift-to-drag ratio. The simulations show that the optimized wing shape and installation angle meet the lift requirements of the carrier aircraft, and the longitudinal stability is improved by adjusting the install position of the wing and the leading edge sweep angle, which is fixed at 15 degrees. The effect of adding flat tails is to increase lift and improve trim and longitudinal stability. Moreover, the upper single-wing layout can improve lateral stability (flaperons are arranged on both sides of the wings for lateral control and increasing lift). The vertical tails, responsible for the yaw stability and control, are placed underneath the fuselage to prevent interference with the target aircraft. The optimized parameters of the carrier aircraft are listed as follows, the total weight of 20 tons, the length of 22 m, the width of 20.2 m, the height of 3.2 m, the cockpit height of 1.8 m, and the lower end of the vertical tail is 1.3 m away from the fuselage. The optimized aerodynamic performances of the carrier aircraft give the maximum lift-to-drag ratio exceeding 8.0, the center of mass position on 55 percent of L (the total length), and the focal position (called X_{ac}) on about 57 percent of L. The longitudinal, lateral, and heading static stability are also proved.

The main work on the design of the compound aircraft focuses on the conception and optimization of the carrier aircraft. In contrast, the configurations and parameters of the target aircraft adopt the general delta-wing layout without specific optimization. The adopted parameters are the length of 15 m, the width of 9.6 m, the height of 1.5 m and the total weight of 20 tons. The inertia of moments are $I_{xx} = 1.5E5\ kg \cdot m^2$ and $I_{yy} = I_{zz} = 1.5E6\ kg \cdot m^2$.

B. VERTICAL TAKE-OFF, HORIZONTAL ACCELERATION, AND SEPARATION

Overall processes of the present scheme for vertical take-off are sketched in Fig. 2, which can be divided into the following main steps (stages). The first stage is the vertical take-off of the compound aircraft. In the beginning, the target aircraft is mounted well upon the carrier aircraft, and its landing gear tires are locked with the locking mechanism. The lift engines start up and lift the compound aircraft to around 1-2 km. Then the next stage is the horizontal acceleration stage. The thrust engines start up and accelerate the compound aircraft to reach a high separation speed to ensure safe separation. During this stage, the lift force of the compound aircraft is provided mainly by the wings of the two aircraft, and the lift engines of the carrier aircraft gradually turn off. As the flight speed reaches the requirement of safe separation (called the pre-separation stage), the angle of attack of the compound aircraft is gradually decreased because a lower angle of attack is conducive to avoiding collision during separation.

The third stage is the separation stage. The initial separation attitude (angle of attack, relative height, and installation angle) of the compound aircraft has been adjusted in the pre-separation stage in order to have the best initial state for separation. The separation begins with the release of the target aircraft, which then moves upward and away from the carrier aircraft. The dynamical variation of aerodynamic force during separation is complicated, and the details will be given in the following sections. When there is no more interference between the target and carrier aircraft, the carrier aircraft flies back and the target aircraft continues to perform its task. It should be noted that the landing of the target aircraft can be achieved either by the conventional landing or by the docking with the carrier aircraft. The latter achieves the goal of vertical landing, which is beyond the scope of this paper.

The aerodynamic coupling between the target and carrier aircraft is essential during the horizontal acceleration and separation stages. It is necessary to estimate the impact of aerodynamic coupling on the lift and drag forces. Furthermore, it is needed to analyze the influence of different initial separation states on the separation process. Therefore, detailed aerodynamic simulations of the aerodynamic

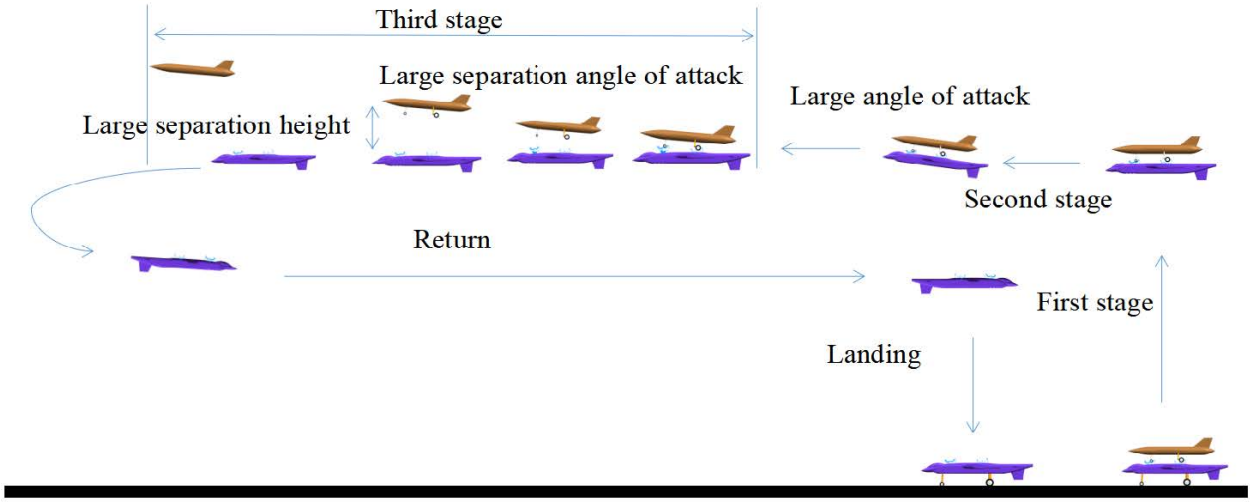

FIGURE 2. Schematic diagram of overall processes of the present scheme.

parameters of the compound aircraft during the horizontal acceleration and separation stages are given in the following sections.

C. NUMERICAL SIMULATION

A cell-centered finite volume scheme is employed to solve the compressible perfect gas Navier-Stokes equation. For turbulence closure, the Reynolds-Averaged-Navier–Stokes (RANS) and the 2-equation realizable k-epsilon turbulence model are used. The AUSM+ spatial discretization scheme is adopted [19], with an implicit lower-upper symmetric Gauss-Seidel scheme for the temporal integration to accelerate convergence [20]. The minmod limiter is used to capture shock, and the viscous terms are discretized using the second-order central differences. As for the unsteady calculations for simulating separation processes, the governing equations are solved using the dual-time-stepping method, and local time stepping with the fourth-order Runge-Kutta scheme is used at the subiteration. Besides, the governing equations are solved in Arbitrary Langrangian-Eulerian framework to deal with the unsteady rigid body motion, and the unstructured overset grid is used in the calculation.

Specifically, as illustrated in Fig. 3, multiple grids overlapped with each other are generated. The grids near the wall are prism cells, and the others are tetrahedral cells. The surface grids of the carrier and target aircraft are shown in the left panel of Fig. 3. As seen in the right panel of Fig. 3, the surface grid number is 250,000 for the carrier aircraft with 30 layers in the boundary layer, and the height of the first layer is 1E-5 m, which satisfies $y_+ < 1$. As a result, a total of 21 million grids are generated to enclose the carrier aircraft. The grid parameters of the target aircraft are listed as follows, 128,000 surface grids, 30 boundary layers with the first grid height equaling 1E-5 m and $y_+ < 1$, and the total grid number is up to 5.35 million. The grid

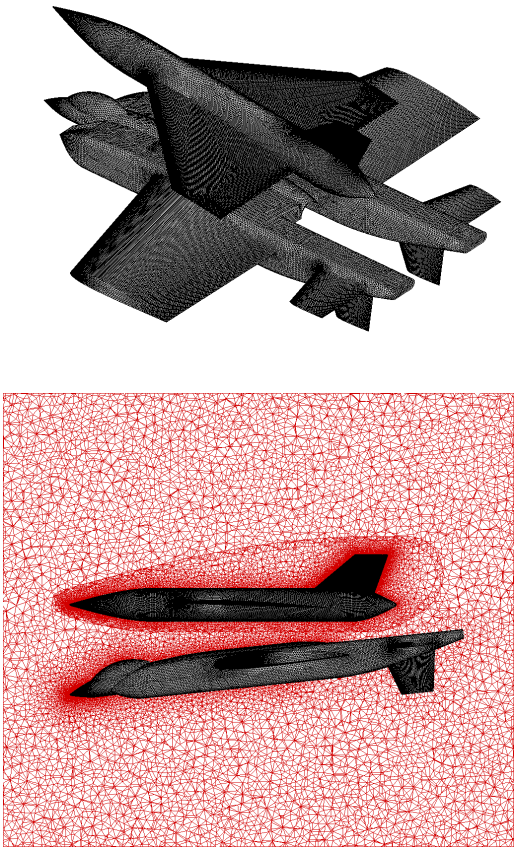

FIGURE 3. Grid of the compound aircraft. (*upper*) surface grid; (*lower*) multiple grids.

independence check is conducted using a denser grid than the above one and refining along the streamwise direction on the body. The relative force coefficients, including the lift and

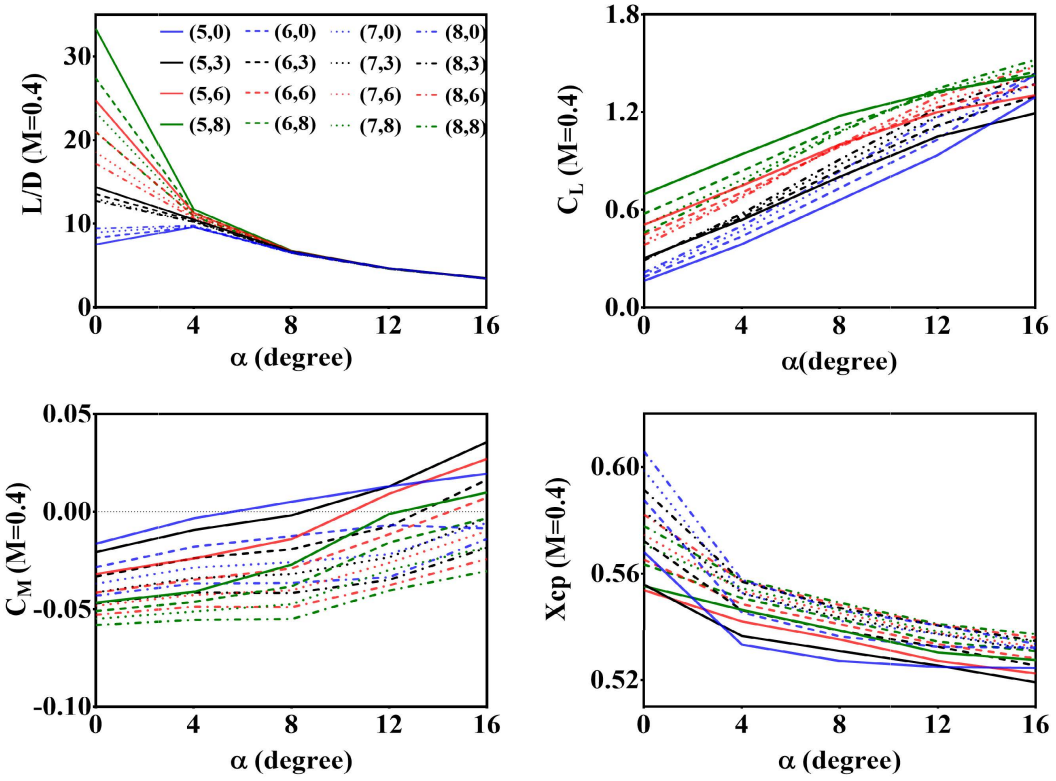

FIGURE 4. The lift-to-drag ratio, lift coefficient, pitch moment, and position of pressure center of the target aircraft in the compound state with Mach number 0.4. The number in parentheses (such as (5,0)) means the installation height H (is 5 m) and installation angle A (is 0°).

drag coefficients and the center of pressure, are very close. Therefore, the above coarser grid is used in the following to save computational costs.

D. AERODYNAMIC PERFORMANCE OF THE COMPOUND AIRCRAFT

The aerodynamic characteristics of the target and carrier aircraft in compound state are simulated based on above simulation method and computational grid. In addition to adjusting the installation angle A (equaling to 0°, 3°, 6°, 8° respectively) and the installation height H (equaling to 5 m, 6 m, 7 m, 8 m respectively) between the two aircraft, different incoming flow conditions are also tested by varying the angle of attack α (concerning the target aircraft) and Mach number M. The above parameters are indicated in Fig. 1 (b). Fig. 4 shows the lift-to-drag ratio (L/D), lift coefficient (C_L), pitch moment (C_M), and center of pressure (X_{cp}) of the target aircraft in the compound flight state with the incoming Mach number of 0.4 and altitude of 2 km.

As seen in Fig. 4, the changes in the aerodynamic parameters of the target aircraft with respect to the installation height H are intriguing. It shows that at a smaller angle of attack with an installation angle equal to 6° or 8°, the lift coefficient of the target aircraft will decrease as installation height increases. The opposite trend is found at a larger angle of attack. Moreover, at a certain angle of attack (hereafter

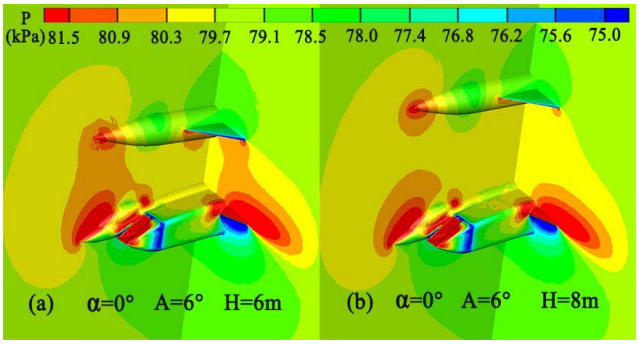

FIGURE 5. Pressure contour diagram for relative height being (a) 6 m and (b) 8 m.

called lift coefficient inflection point, α_H), the lift coefficients at different installation heights are almost the same. In the case of an angle of attack higher than α_H, the lift coefficient increase with installation height; this is in line with the intuitive law of physics. In the case of an angle of attack lower than α_H, as installation height increases, the lift coefficient of the target aircraft decreases, so as the lift-to-drag ratio. The reason is mainly due to aerodynamic coupling between two aircraft. By analyzing the pressure contour diagram in the case of the angle of attack lower than α_H (see Fig. 5; the simulation condition is the angle of attack 0° for the target aircraft with Mach number 0.4 and installation angle 6°),

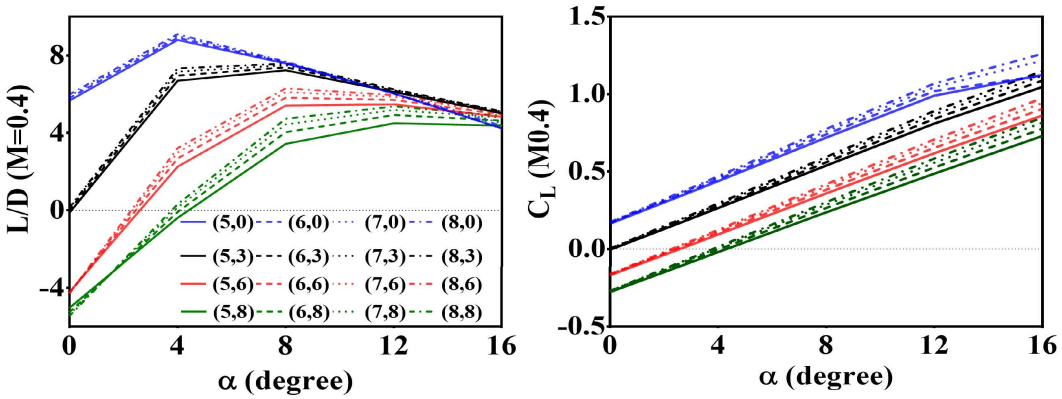

FIGURE 6. Lift-to-drag ratio and lift coefficient for the compound aircraft with Mach number 0.4. The number in parentheses (such as (5,0)) means the installation height H (is 5 m) and installation angle A (is 0°).

it can be seen that high-pressure regions show on the nose and wing-body junction of the carrier aircraft. The appearance of those high-pressure areas increases the lift of the target aircraft. As the relative height increases (see Fig. 5), this area is far from the target aircraft and has a smaller effect on lift increase. As a result, the lift coefficient of the target aircraft goes down with relative height increases.

As also seen in Fig. 4, the aerodynamic parameters of the target aircraft vary significantly with the installation angle A. A larger installation angle gives a greater lift coefficient, lift-to-drag ratio, and α_H. For instance, α_H is $-12.5°$, $1.0°$, $7.9°$ and $11.0°$ when the installation angle is $0°$, $3°$, $6°$ and $8°$, respectively. The ideal situation during the separation stage is that the lift coefficient of the target aircraft (slightly) increases as the separation height increases, which appears in the flight angle of attack larger than α_H. Therefore the appearance of α_H plays an important role in the lift variation during the separation stage, which needs to be considered carefully.

Furthermore, the aerodynamic performance of the compound aircraft is given in Fig. 6, which shows the lift-to-drag ratio (L/D) and lift coefficient (C_L) of the compound aircraft with Mach number 0.4. The cases of installation angle A (equals to $0°$, $3°$, $6°$, $8°$, respectively) and the installation height H (5 m, 6 m, 7 m, 8 m) between the carrier and target aircraft are investigated. It can be found that when the installation height is fixed, the lift coefficient of the compound aircraft decreases with the increase of the installation angle. The influence of the installation height on the lift-to-drag ratio is much smaller than that of the installation angle. As the angle of attack increases, the lift and drag coefficients increase. As a result, the lift-to-drag ratio reaches the maximum at a certain angle of attack, which increases with the installation angle. Moreover, it can be seen that a smaller installation angle leads to a larger maximum lift-to-drag ratio. Based on the above analysis, the flight is more economical when the compound aircraft employs a larger installation height and a smaller angle of attack in a small installation angle. It should be noted that increasing the installation height of the target aircraft will inevitably increase the weight in the design of the locking mechanism (from the perspective of structural mechanics). It will also increase the torsion resistance and compression resistance of the locking mechanism.

The lifts of the target, carrier, and compound aircraft under different conditions are shown in Fig. 7 for Mach number 0.4. The lift force pointing upward is positive. From the data of Fig. 7, one can approximately estimate the feasible regions of separation, which are sketched in Fig. 8 for Mach number 0.4 under different values of A, H, and α.

The attitude adjustment should be made in the pre-separation stage to ensure the parameters fall within the feasible separation region. As a rule of thumb, the feasible region is defined as the area satisfying the following conditions: the total lift is enough to support the compound aircraft; the target aircraft has a lift greater than its gravity for moving upward; the lift of the carrier aircraft can not be much small (depending on the performance of the aircraft control system and the flight altitude) than its gravity and can not be larger than the lift of the target aircraft.

Specifically, as shown in Fig. 7, under the condition of H = 5 m, A = $8°$ and M = 0.4, all the reported angles of attack can satisfy the above rules of separation for the target aircraft. But the total lift of compound aircraft is enough only when the angle of attack is larger than $9.1°$. Moreover, the lift of the carrier aircraft is less than its gravity when the angle of attack is smaller than $12°$. If the separation occurs with the angle of attack smaller than $12°$, the carrier aircraft will descend at a falling speed after separation and cause a challenge to the control system of the carrier aircraft. As also shown in Fig. 7, the lift variation to the angle of attack is faster for the carrier aircraft than the target aircraft. Thus at a certain angle of attack, the lift of the carrier aircraft exceeds the lift of the target aircraft. This particular angle of attack is then defined as the maximum separation angle of attack. Beyond this angle of attack, the separation will result in a collision and failure.

In Fig. 8, the minimum angles of attack of the carrier and target aircraft (for successful separation) with respect to installation angle are given, as well as the maximum

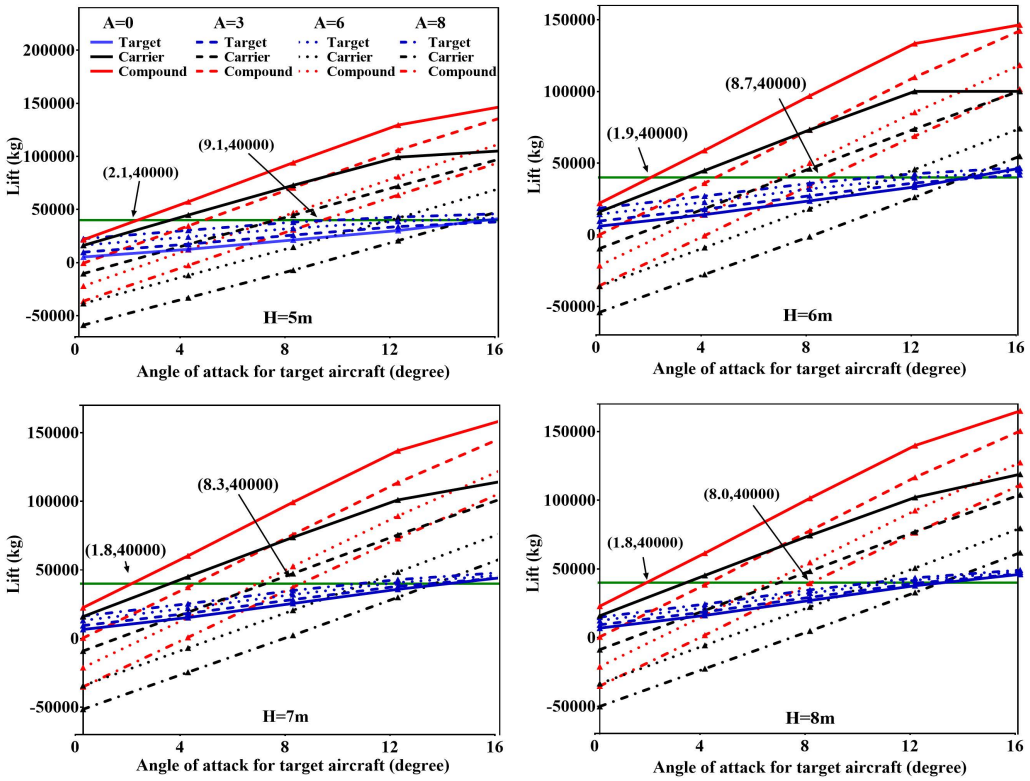

FIGURE 7. The lift (kg) of the target, carrier, and compound aircraft with different H at Mach number 0.4 and altitude of 2 km.

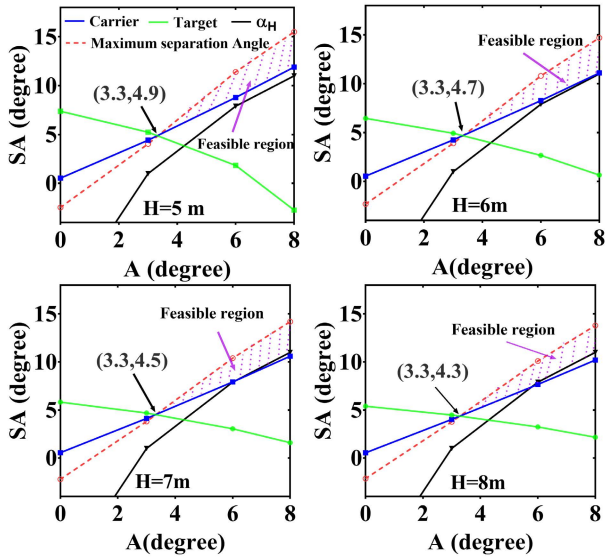

FIGURE 8. Feasible regions of separation with Mach number 0.4 at an altitude of 2 km, where SA is the separation angle of attack.

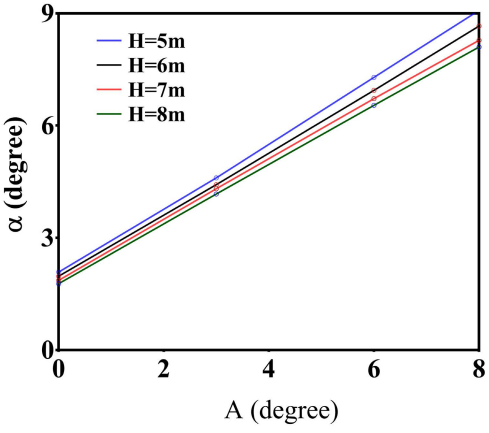

FIGURE 9. Relationship between the installation angle A and the angle of attack α for maintaining the total lift to be 40 tons.

separation angle. It is seen from Fig. 8 that the smaller the installation height, the larger the feasible area. In addition, it is important to maintain the compound aircraft flying at a given altitude before separation. Fig. 9 shows the relationship between the installation angle A and the angle of attack α with different installation height H for maintaining the total lift to be 40 tons (the weight of the compound aircraft). It can be seen from the figure that the installation angle A and the angle of attack α basically maintain a linear relationship.

E. UNSTEADY AERODYNAMIC CHARACTERISTICS DURING THE SEPARATION STAGE

CFD/RBD method is used to calculate the unsteady separation process. The governing equations are solved in Arbitrary

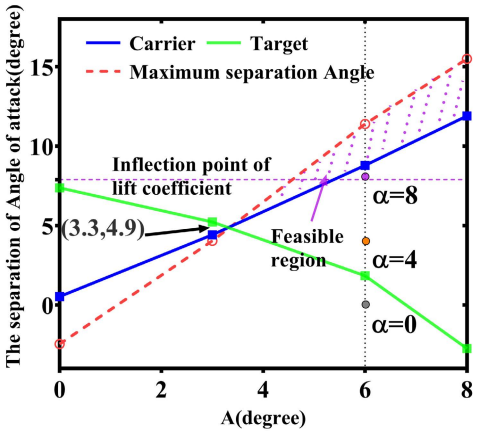

FIGURE 10. Three simulation cases are indicated in the diagram of the feasible region with H=5 m.

Langrangian-Eulerian framework to deal with the unsteady rigid body motion. The flow computation and the trajectory simulation are decoupled over a small time step. At each step, the flow computation is carried out until the flowfield reaches the steady-state solution. Then, the 6-DOF solver is applied to obtain the new location of the target aircraft.

Although the feasible region of separation obtained in the last subsection guarantees the safe separation at the moment of separation, two issues still need to be considered during the separation process. The first one is the influence of α_H on the target aircraft during the dynamic separation process. The second one is to ensure safety when the lift of the carrier aircraft is slightly less than its weight. Concerning the first issue, α_H is related to the lift coefficient, and the lift coefficient at the angle of attack near α_H is almost not affected by the installation height. As shown in Fig. 8, curves of α_H are added. Above the curve is the area where the lift coefficient increases as the angle of attack increases. To verify whether the dynamical separation process complies with the above analysis, three separation conditions are calculated. The simulation conditions are listed as follows: the flight altitude is 2 km, the Mach number is 0.4, H equals 5 m, A equals 6°, and the attack angle is 0°, 4° and 8°, respectively. The lift coefficient inflection point α_H is 7.9° under the above conditions.

The simulation cases are indicated in Fig. 10, as well as the lift coefficient inflection point. In the first case, the separation angle of attack α is 0°, and the separation fails because of insufficient lift. α is 4° in the second case, where the target aircraft can be separated. However, since the angle of attack is much smaller than α_H, the target aircraft would first move upward and then go down, which leads to the failure of separation. α is 8° in the third case, which is greater than α_H, and the target aircraft separates successfully.

Fig. 11 shows the variation of the target aircraft during the dynamical separation process of the above three cases. The left panel of Fig. 11 shows the variation of the Z-direction coordinate during the separation process. It can be seen that the separation is failed when α equaling 0° due to the insufficient lift of the target aircraft so that it falls down immediately after separation. With increasing α to 4°, the lift of the target aircraft is greater than its weight after separation. However, as the Z-coordinate increases, the lift drops significantly because the angle of attack is smaller than α_H in this case. Moreover, the pitching moment is negative, meaning that the aircraft is nose-down during separation. It is dangerous if there is no further operation to pull the aircraft up. On the contrary, 8° is more close to α_H, so it can be expected that there is almost no loss of lift as the relative height of two aircraft increases. And the lift at this higher angle of attack is more considerable. Therefore, the separation is successful. The right panel of Fig. 11 shows the temporal variations of the pitching moment and lift of the target aircraft when α is 8°. Due to the aerodynamic interference, the target aircraft shows a nose-down pitching moment. Thus, the effective angle of attack decreases, and the lift also gradually decreases. Generally, after separation, the operation start-up time is around one to two seconds. If the target aircraft can move up to a safe distance within this time interval, the separation can be considered successful. The above calculations show that the angle of attack at the moment of separation should be a large value to ensure the successful separation. In other words, the compound aircraft should appropriately increase the angle of attack during the pre-separation stage.

The pressure contour diagrams at different time steps are shown in Fig. 12 for α equaling 8° with Mach number 0.4. It can be seen that the target aircraft gains a nose-down pitching moment during the separation process. The aerodynamic coupling disturbs the flow field between two aircraft. Moreover, the lift of the carrier aircraft is slightly lower than its gravity and is in a downward falling state. If the carrier aircraft is appropriately controlled (the details are beyond the scope of the work), the falling down of the carrier aircraft is conducive to separation.

III. DESIGN OF THE UNMANNED CARRIER AIRCRAFT

The proposed scheme is tested using aerodynamic numerical simulation in the previous section. The simulated dynamic separation process with appropriate installation parameters (A and H) and flight parameters (α and airspeed) gives successful separation. The above results theoretically prove the feasibility of the present scheme, and the next step is to validate the present scheme through flight tests. A fixed-wing aircraft model with the delta-wing layout is chosen as the target aircraft, and an unmanned aircraft is designed specially as the carrier aircraft in the flight test. It is hard to fully follow the designed configuration (reported in the last section) of the carrier aircraft because of limited funding, so a compromise solution is using four lift propellers to provide lift during the vertical take-off stage.

The actual models for the flight test are shown in Fig. 13. Specifically, the take-off weight of the target aircraft (see Fig. 13 (c)) is 3.2 kg, with a length of 1630 mm and a wingspan of 1080 mm. In the actual flight test, it can be

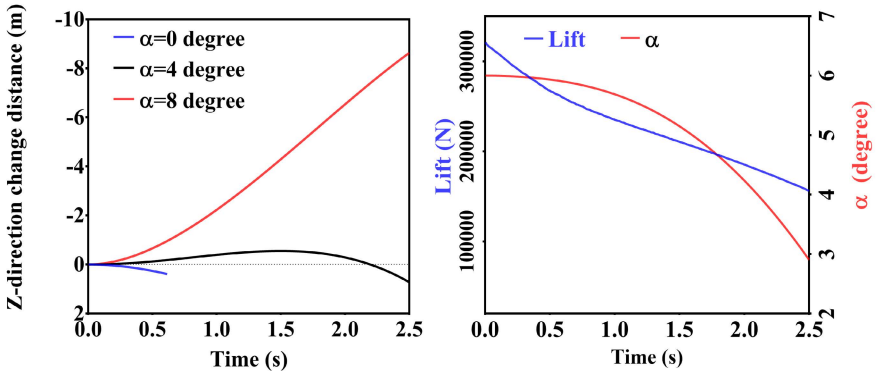

FIGURE 11. Variation of Z-direction coordinate under three different angles of attack (left panel), and variations of lift and angle of attack with respect to time when α is 8° (right panel).

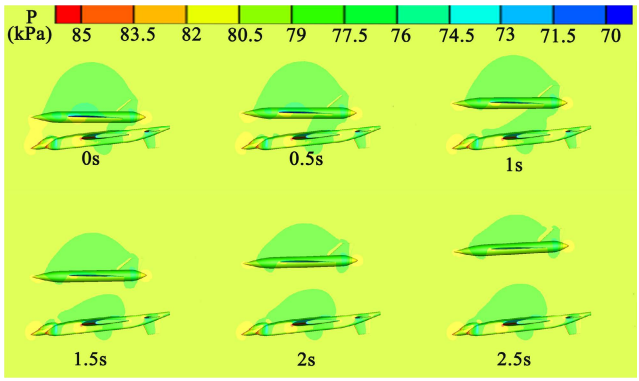

FIGURE 12. The pressure contour diagram of the $\alpha = 8°$ case.

seen from Fig. 14 (a) that the target aircraft can take off at an airspeed of 20.6 m/s and ground speed of 18.1 m/s without any take-off control rudder amount. On the contrary, as seen from Fig. 14 (b), the target aircraft can take off at an airspeed of 10.5 m/s and ground speed of 10.95 m/s with the maximum control rudder amount. The take-off speed of the target aircraft determines the designed flight speed of the unmanned carrier aircraft, which is critical in selecting the thrust engine.

The designed unmanned carrier aircraft is shown in Fig. 13 (a), which is capable of vertical take-off and horizontal acceleration and is equipped with a reusable connecting mechanism. Based on the quadrotor UAV with four lift propellers (providing lift for vertical take-off), the present unmanned carrier aircraft adds a tail thrust propeller, which provides the horizontal thrust during the horizontal acceleration stage. As for the connection between the target and carrier aircraft, the current approach is to connect the landing gear tires of the target aircraft by using the connecting mechanism mounted on the unmanned carrier aircraft, as shown in Fig. 13 (b).

Specifically, as shown in Fig. 13 (a), the unmanned carrier aircraft contains four parts, i.e., the power system, the body structure, the connecting mechanism, and the control system. Its total weight is 20.20 kg, and the body coordinate system

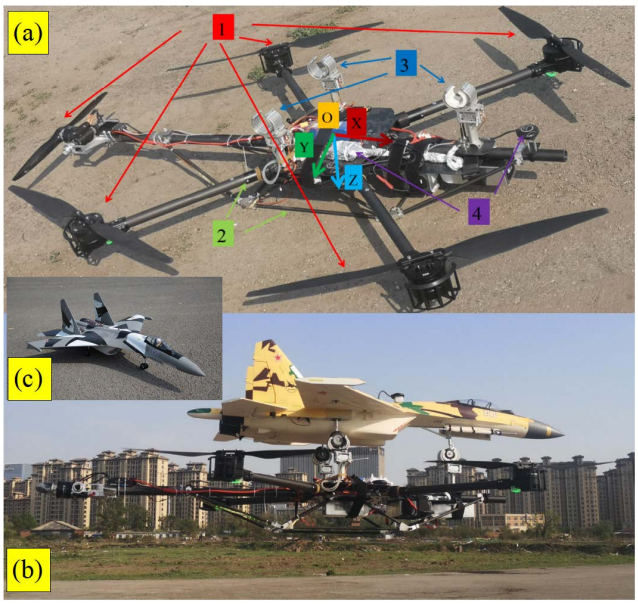

FIGURE 13. Actual models of (a) the unmanned carrier aircraft, (b) the compound aircraft, and (c) the target aircraft.

OXYZ is located at the center of the four lift propellers. The different parts of the unmanned carrier aircraft will be introduced in the following.

A. THE POWER SYSTEM AND AERODYNAMIC ANALYSIS

As shown in Fig. 13 (a), the power system of the unmanned carrier aircraft uses four lift propellers (which are arranged symmetrically) to generate lift. Besides that, a horizontally installed thrust propeller is arranged to create thrust. The lift propeller selects the type of Hobbywing X8, and its weight and diameter are 1.04 kg and 762 mm, respectively. A single set's maximum instantaneous lift force is 150 N (with a rotational speed of 4800 rpm). The power component used for the thrust propeller is a XM6360EA brushless motor with 20 × 10E high-speed propeller, which generates a maximum thrust of 141.92 N at a speed of 8202 r/min. The weight and diameter of the thrust propeller are 0.635 kg and 508 mm, respectively.

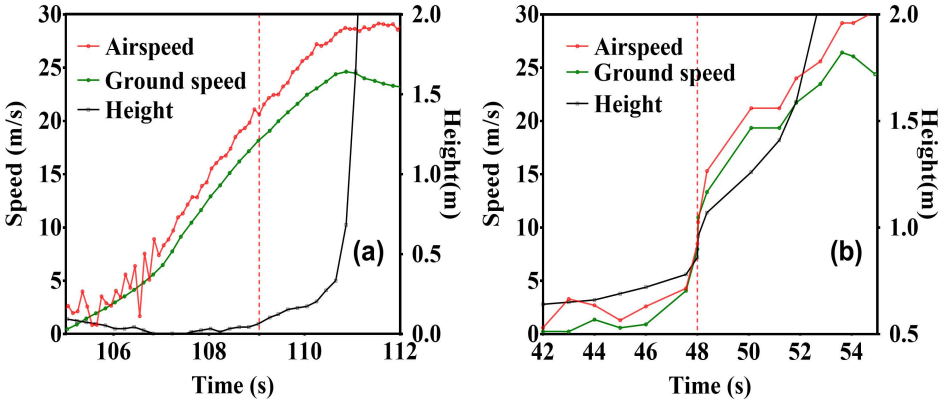

FIGURE 14. Altitude and speed of the target aircraft during the take-off process (a) without control rudder amount and (b) with maximum control rudder amount.

According to nominal parameters of the power system, the maximum instantaneous lift of the unmanned carrier aircraft is 600 N, while the lift for long-time operation is 196 $\sim$ 274.4 N. The flight test requires the experimental time to be larger than five minutes. Thus, four 6S, 10000 mAh lithium batteries are used to supply electric power. A single lithium battery weighs 1.37 kg, so the total weight of the power system plus batteries counts 10.275 kg.

When all the propellers (four lift propellers plus the thrust propeller) are operating, the aerodynamic coupling among them will affect the force generated by each propeller. In order to study the aerodynamic coupling effect, numerical simulations are calculated. The simulated scenario is that the carrier aircraft initially hovers at 300 m altitude, and the thrust propeller does not start yet. According to the total weight of the carrier aircraft, each lift propeller should produce an average lift of 49.49 N. As the thrust propeller starts and reaches the maximum speed, the trends of the force generated by all five propellers with respect to airspeed are shown in Fig. 15.

In Fig. 15 (a), it can be seen that if the thrust propeller (hereafter called No. 5 propeller) reaches the maximum thrust (with a rotational speed of 8202 rpm), the four lift propellers show different trends in the lift as the airspeed of the unmanned carrier aircraft increases. Since the No. 1 and No. 2 lift propellers arranged in front are farther away from the thrust propeller, the effect of aerodynamic coupling on them is more negligible. Whereas the lift propellers No. 3 and No. 4 at the rear are closer to the thrust propeller, thus the influence of aerodynamic coupling is significant. The lift of propellers No. 3 and 4 decreases at the smaller airspeed and then increases gradually (showing a minimum lift point) with airspeed increasing.

The thrust propeller can provide the maximum thrust of 141.92 N according to the nominal parameter, which is validated by the CFD result of 141.99 N. The '5-alone' curve in Fig. 15 (a) indicates the lift variation, which first increases and then decreases, of isolated thrust propeller with respect to airspeed. By comparing the curves '5' and '5-alone', it can be seen that the influence of aerodynamic coupling should be considered, which decreases the thrust.

In order to keep the unmanned carrier aircraft flying at a constant altitude during the acceleration stage, the rotational speed of the lift propellers should reduce to maintain the balance between lift and gravity. The variations in the rotational speed of the lift propellers to maintain a fixed altitude are shown in Fig. 15 (b).

B. STRUCTURE OF THE UNMANNED CARRIER AIRCRAFT

The body structure of the unmanned carrier aircraft is designed to satisfy the requirement of strength and stiffness. The carbon fiber compound material is used because of its high strength and low density. Using carbon fiber sheets and tubes as the main body structure is easy to process and assemble. The optimized fuselage skeleton structure is shown in Fig. 16. Beams 1, 2, 3 and 4 shown in Fig. 16 (a) are the mounting arms of the four lift propellers, and beam 5 is the mounting arm of the thrust propeller. Beam 6 holds the connecting mechanism for the front landing gear tire of the target aircraft, and truss 7 is a set of reinforcing truss structures to prevent the large deformation of beams 5 and 6. Fig. 16 (b) shows the schematic diagram of the reinforcing truss structure. Binary rotation mechanism 8 (see the zoom view in Fig. 16 (c)) is designed to realize the rotation of the motor along the XOZ plane (shown in Fig. 13 (a)). The servo (the yellow part in Fig. 16 (c)) drives a linkage mechanism to make beam 9 (installing the thrust motor) rotate around its circle center.

The body frame structure is divided into 343703 grids with eight nodes hexahedron elements for structural finite element analysis. The lift forces of beams 1, 2, 3, and 4 are set to 50 N, and the amount of deformation generated at the end of the beam is 1.94 mm. The gravity 7 N generated by the motor is set on beam 9, and the maximum deformation at the end of beam 9 is 1.23mm. Among them, beams 1-9 and the two connecting plates in the middle use carbon fiber materials,

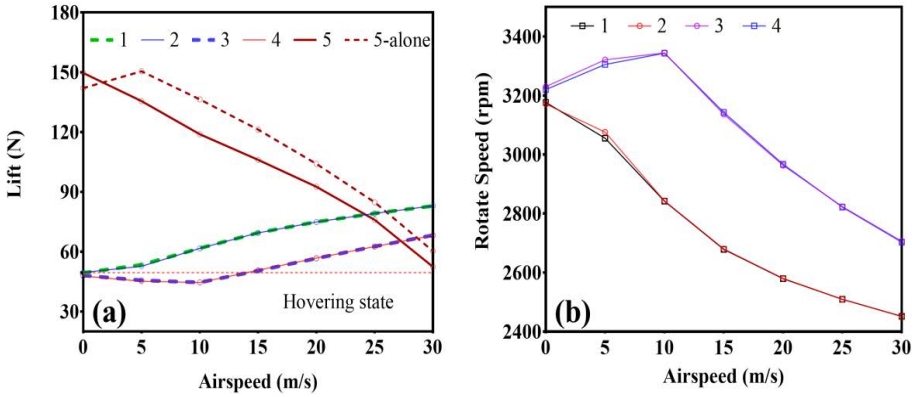

FIGURE 15. Aerodynamic simulation of the unmanned carrier aircraft during the horizontal acceleration stage. (a) Forces of the lift propellers (with a rotational speed of 3175 rpm) and the thrust propeller (with a rotational speed of 8202 rpm); (b) rotational speed of the lift propellers.

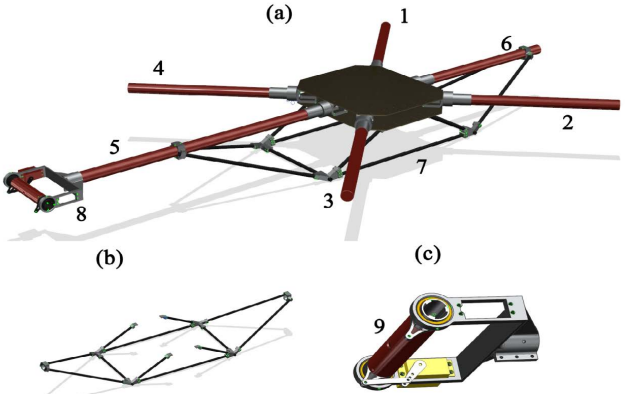

FIGURE 16. The structure of the unmanned carrier aircraft. (a) Oblique view of the body structure; (b) truss structure of part 7; (c) zoom view of the binary rotation mechanism 8.

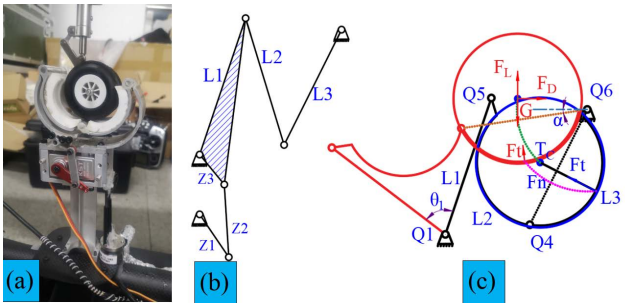

FIGURE 17. The connecting mechanism. (a) Actual model; (b) design schematic; (c) the moving trajectory of the landing gear tires at connected (black) and separated states (red).

and the rest of the connecting parts are made of aviation aluminum alloy. The present structure of the carrier aircraft shows high stiffness and strength in the simulation, and it also demonstrates good reliability in the flight and separation experiments (see below).

C. THE CONNECTING MECHANISM

The design of the connection mechanism is better to suit multiple types of target aircraft, and it is also essential to ensure stable connection and opening when operating. Generally, three landing gears and circle tires (isosceles triangle distribution) are the characteristics of most fixed-wing aircraft. Therefore, locking the landing gear tires of the target aircraft by the connecting mechanism of the unmanned carrier aircraft is a universal solution.

The present connecting mechanism with a white conformal frame (designed for different tire sizes) and the black landing gear tire are shown in Fig. 17 (a). The design schematic of the connecting mechanism is given in Fig. 17 (b). To better connect and fix the round tire of landing gear, L2 and L3 are designed as round arc type conformal frames. When the connecting rod L1 moves to the right, it drives L2 and L3 to move and clamp the tire. The connecting mechanism adopts two individual four-bar linkage schemes. The first one is composed of rods Z1, Z2, and Z3, and the frame is used as the power output. The second one is composed of L1, L2, and L3, and the frame performs the connecting and separating operations. The power is provided by a high-torque servo (KST-BLS825), and the servo parameters are shown in Table 1.

TABLE 1. Parameters of servo KST BLS825.

Torque	35 kg · cm
Weight	70 g
Rotational speed	0.11 sec/60°
Voltage	8.4 V
Stroke	±60°
Signal	1520 us/333Hz

As shown in Fig. 17 (c), the movement of the rod Z1 drives the rod (Z2, Z3, L1, L2, L3), and the connection mechanism is opened. The landing gear tire follows L3 around the Q6 point. The T_C curve is the motion trajectory of the tire center, and the Fn curve is the trajectory of the contact point. The landing gear tires of the target aircraft will separate in the direction of the combined force (aerodynamic drag F_D, aerodynamic lift F_L, gravity G, and ejection force Ft). The ejection force has less influence in the actual test and is ignored.

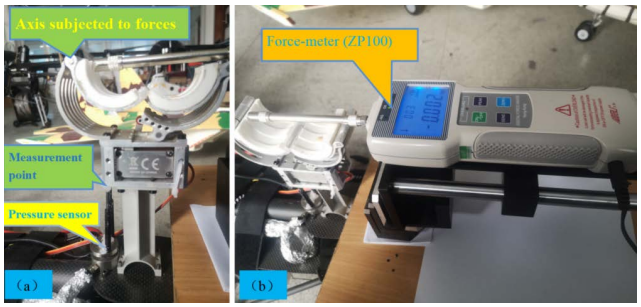

FIGURE 18. Testing the collected values of the pressure sensor.

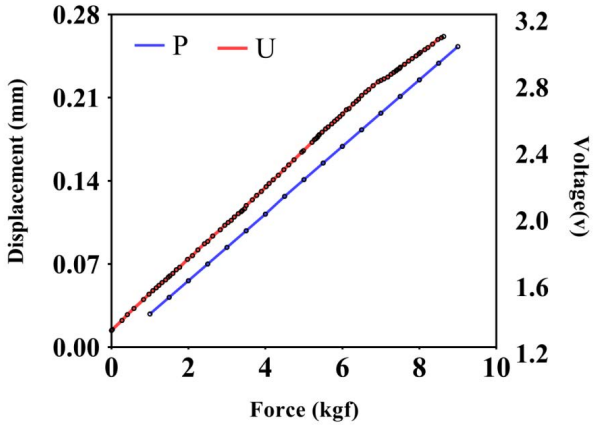

FIGURE 19. Simulated and tested displacement when the support bar is subjected to horizontal force.

A pressure sensor (with output signal 0-3.3 V, range 0-50 kg, accuracy within 0.1%), installed on the connecting mechanism of the front landing gear (see Fig. 18 (a)), is used to collect the force from the deformation of the support bar. Meanwhile, the data is transmitted in real-time to the ground station. Testing of this pressure sensor under horizontal forcing is shown in Fig. 18.

It is known that the vertical displacement (P) of the measurement point is proportional to the electrical signal (U), i.e., $P \propto U$. Through the finite element method simulation, as shown in the P curve in Fig. 19, the displacement (P) is proportional to the horizontal thrust force (Fp). In the actual test, the horizontal thrust force (Fp) is applied through the digital force meter ZP100 (with range 0-10 kgf and accuracy within 0.1 N) shown in Fig. 18 (b). The relationship between the horizontal thrust force and the voltage signal is shown as the U curve in Fig. 19. The testing result is consistent with numerical simulation.

D. DYNAMICS MODEL AND THE CONTROL SYSTEM

1) KINEMATICS AND DYNAMICS OF THE UNMANNED CARRIER AIRCRAFT

There exist differences between the present unmanned carrier aircraft and the traditional quadrotor UAV [21]–[23], including the addition of a two-dimensional rotating thrust propeller at the rear. Moreover, the addition of the connecting mechanism and truss structure makes the unmanned carrier aircraft have only XOZ symmetry structurally. In order to enhance the heading stability of the unmanned carrier aircraft, the mounting angle of the lift propeller is deviated from the horizontal plane for an angle of ξ, as shown in Fig. 20. Although the lift decreases slightly by doing so, the additional moment around the Z-axis is conducive to enhancing the heading stability.

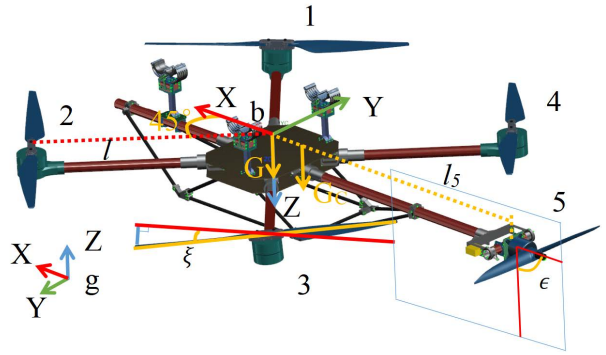

FIGURE 20. Illustration of parameters of the unmanned carrier aircraft.

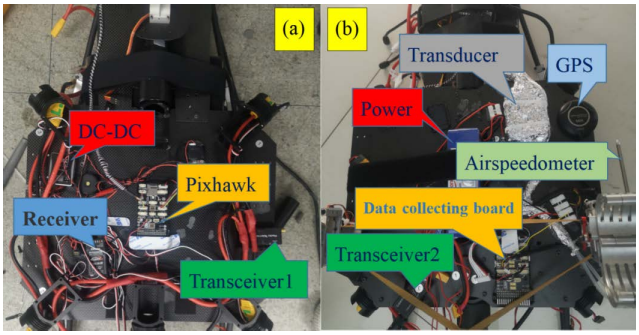

FIGURE 21. (a) Hardware components of the control system and (b) the data acquisition system.

The parameters of the unmanned carrier aircraft are indicated in Fig. 20, where bXYZ is the body coordinate system, gXYZ is the geodetic coordinate system, G is the gravity vector of the unmanned carrier aircraft in the body coordinate system, l is the arm length of the lift propeller, ξ is the rotation angle of the lift propeller around the mounting axis, l_5 is the arm length of the thrust propeller, and ϵ is the rotation angle of the thrust propeller around the rotation axis.

The general form of the kinematics of the unmanned carrier aircraft (similar to the derivation of quadrotor [22], [23]) is given as follows,

$$\begin{bmatrix} \dot{P} \\ \dot{\eta} \end{bmatrix} = \begin{bmatrix} R_{b-g} & 0_{3\times3} \\ 0_{3\times3} & T \end{bmatrix} \begin{bmatrix} V \\ \omega \end{bmatrix}, \tag{1}$$

and the general equation of the dynamical model is

$$\begin{bmatrix} \dot{V} \\ \dot{\omega} \end{bmatrix} = \begin{bmatrix} -S(\omega)V \\ -J^{-1}S(\omega)J\omega \end{bmatrix} + \begin{bmatrix} \mathrm{diag}\left(\frac{1}{m}, \frac{1}{m}, \frac{1}{m}\right) & 0_{3\times3} \\ 0_{3\times3} & J^{-1} \end{bmatrix} \begin{bmatrix} F \\ M \end{bmatrix}, \tag{2}$$

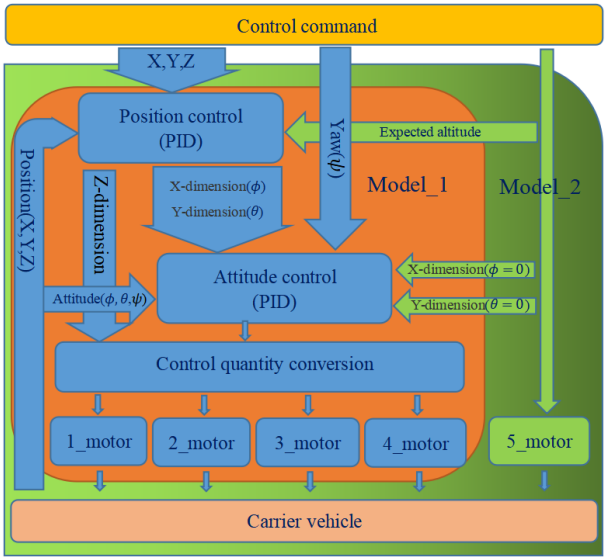

FIGURE 22. Control logic diagram of the unmanned carrier aircraft, where Model 1 is vertical take-off control mode and Model 2 is horizontal acceleration flight mode.

where m is the total mass of the carrier aircraft, $P = [x, y, z]^T$ is the position of the carrier aircraft in the geodetic coordinate system, $\eta = [\phi, \theta, \psi]^T$ is the attitude angle of the carrier aircraft (roll angle ϕ, pitch angle θ, yaw angle ψ), $V = [u, v, w]^T$ is the speed of the carrier aircraft in the body coordinate system, $\omega = [p, q, r]^T$ is the angular velocity of rotation of the carrier aircraft in the body coordinate system, $S(\omega) = \begin{bmatrix} 0 & -r & q \\ r & 0 & -p \\ -q & p & 0 \end{bmatrix}$ is oblique operator matrix and (3), as shown at the bottom of the next page, is the conversion matrix from body to geodetic coordinate systems. $J = \begin{bmatrix} I_x & -I_{xy} & -I_{zx} \\ -I_{xy} & I_y & -I_{yz} \\ -I_{zx} & -I_{yz} & I_z \end{bmatrix}$ is the rotational inertia of the carrier aircraft, where $I_{xy} = I_{yz} = 0$, and $T = \begin{bmatrix} 1 & \sin\phi\tan\theta & \cos\phi\tan\theta \\ 0 & \cos\phi & -\sin\phi \\ 0 & \frac{\sin\phi}{\cos\theta} & \frac{\cos\phi}{\cos\theta} \end{bmatrix}$.

The force F and moment M of the carrier aircraft in the body coordinate system are

$$\begin{aligned} F &= F_L + F_D + G \\ M &= M_L + M_T + M_{\text{inv}}, \end{aligned} \tag{4}$$

where (5), as shown at the bottom of the next page, is the component of the force generated by the propeller in the body coordinate system (k_i is the lift coefficient, Ω_i is the rotor speed). $F_D = \begin{bmatrix} -C_d V_k^2 \cos\alpha\cos\beta \\ C_d V_k^2 \sin\beta \\ C_d V_k^2 \sin\alpha\cos\beta \end{bmatrix}$ is drag force (C_d is the drag coefficient, α is the angle of attack of the unmanned carrier aircraft, β is side slip angle), $G_b = \begin{bmatrix} G\sin\theta \\ -G\cos\theta\sin\phi \\ -G\cos\theta\cos\phi \end{bmatrix}$ is the component of gravity of the unmanned carrier aircraft in the body coordinate system. (6), as shown at the bottom of the next page, is the moment generated by the lift force, $M_T = \begin{bmatrix} 0 \\ -m_T g l_5 \cos\theta\cos\phi \\ m_T g l_5 \cos\theta\sin\phi \end{bmatrix}$ is the moment component generated by the tail motor in the body coordinates, and (7), as shown at the bottom of the next page, is the counter-torque moment generated by each propeller (k_{i_inv} is the counter-torque coefficient).

2) THE CONTROL SYSTEM OF THE UNMANNED CARRIER AIRCRAFT

The core of the control system is developed based on the pixhawk open-source drone hardware, and the fundamental hardware components are shown in Fig. 21. The control board installed inside the aircraft (see Fig. 21 (a)) controls the flight status of the aircraft and receives remote commands from the ground. Transceiver 1 transmits flight data, such as the attitude and altitude of the unmanned carrier aircraft, to the ground station. Fig. 21 (b) shows the installed data acquisition board, which collects the airspeed and pressure sensor data of the unmanned carrier aircraft and then transmits them to the ground station through transceiver 2 in real-time.

By analyzing the data of the carrier aircraft, the control mode is switched between vertical take-off and horizontal acceleration modes. The vertical take-off mode uses the four lift propellers for power output to achieve vertical take-off and attitude control. Horizontal acceleration flight mode is used after ensuring the carrier aircraft is lifted to the desired altitude. In the latter mode, four lift propellers are mainly used to control the attitude, while the tail thrust propeller is activated to accelerate the carrier aircraft. The four lift propellers adjust the attitude so that the carrier aircraft can meet the attitude requirements of separation.

The control logic diagram of the unmanned carrier aircraft is shown in Fig. 22. The PID algorithm is used for present attitude and altitude control considering its robustness under significant external disturbance, especially the disturbance at the moment of start-up of the tail propeller and the moment of separation.

3) FLIGHT TEST OF THE UNMANNED CARRIER AIRCRAFT

In order to test the flight performance of the present carrier aircraft, a test flight was conducted at a deserted airport in Changchun, China, and the wind speed varied from 2 m/s to 5 m/s during the test time. In the flight test, the data related to the horizontal acceleration of the unmanned carrier aircraft were obtained. The airspeed and the ground speed of the unmanned carrier aircraft during the acceleration stage are shown in Fig. 23 (a). It can be seen that the unmanned carrier aircraft reached an airspeed of 28m/s after

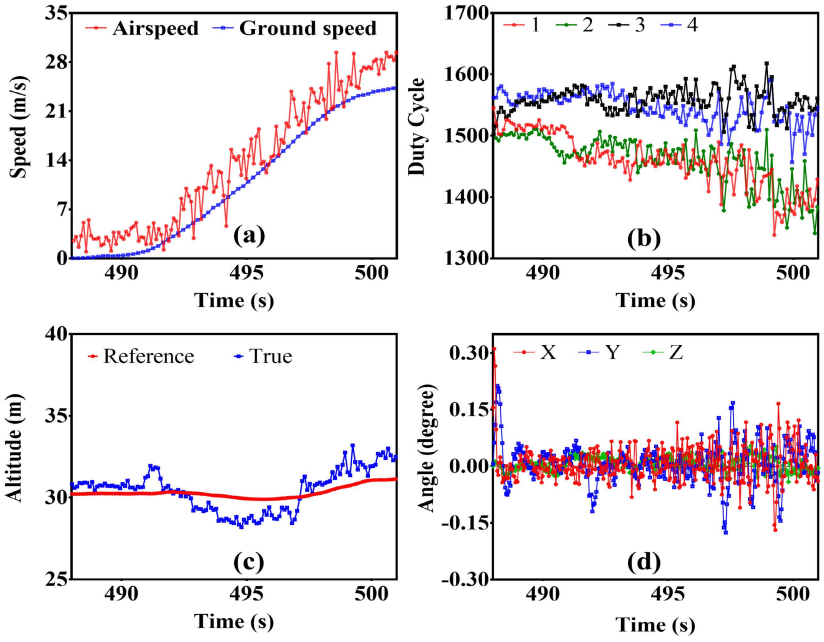

FIGURE 23. Data obtained during the acceleration stage of the carrier aircraft. (a) Speed variation with respect to time; (b) duty cycle of four lift propellers; (c) altitude variation; (d) attitude variation.

70 seconds of acceleration. The duty cycle of the four lift propellers is shown in Fig. 23 (b). The results are consistent with the trend and range of the propeller obtained from the numerical simulation. Moreover, the altitude and attitude variation curves are shown in Fig. 23 (c) and Fig. 23 (d), respectively. Although there is fluctuating up and down due to aerodynamic interference, the present control loops adjust the unmanned carrier aircraft to fly at the desired altitude and altitude.

As seen in Fig. 24 (b), the flight trajectory (the red line) during the acceleration stage is a straight line with high navigational stability, and the flying direction was opposite to the wind direction. The 0 m/s ground speed means the unmanned carrier aircraft is hovering. In Fig. 24 (a), it can

$$R_{b-g} = \begin{bmatrix} \cos\psi\cos\theta & \cos\psi\sin\theta\sin\phi - \sin\psi\cos\phi & \cos\psi\sin\theta\cos\phi + \sin\psi\sin\phi \\ \sin\psi\cos\theta & \sin\psi\sin\theta\sin\phi + \cos\psi\cos\phi & \sin\psi\sin\theta\cos\phi - \cos\psi\sin\phi \\ -\sin\theta & \cos\theta\sin\phi & \cos\theta\cos\phi \end{bmatrix} \tag{3}$$

$$F_L = \begin{bmatrix} \frac{\sqrt{2}}{2}\left(-k_1\Omega_1^2 - k_2\Omega_2^2 + k_3\Omega_3^2 + k_4\Omega_4^2\right)\sin\xi + k_5\Omega_5^2\sin\epsilon \\ \frac{\sqrt{2}}{2}\left(k_1\Omega_1^2 - k_2\Omega_2^2 - k_3\Omega_3^2 + k_4\Omega_4^2\right)\sin\xi \\ \left(k_1\Omega_1^2 + k_2\Omega_2^2 + k_3\Omega_3^2 + k_4\Omega_4^2\right)\cos\xi + k_5\Omega_5^2\cos\epsilon \end{bmatrix} \tag{5}$$

$$M_L = \begin{bmatrix} \frac{\sqrt{2}}{2}l\sin\xi\left(-k_1\Omega_1^2 + k_2\Omega_2^2 + k_3\Omega_3^2 - k_4\Omega_4^2\right) \\ \frac{\sqrt{2}}{2}l\sin\xi\left(k_1\Omega_1^2 + k_2\Omega_2^2 - k_3\Omega_3^2 - k_4\Omega_4^2\right) - l_5k_5\Omega_5^2\cos\epsilon \\ l\sin\xi\left(k_1\Omega_1^2 - k_2\Omega_2^2 + k_3\Omega_3^2 - k_4\Omega_4^2\right) \end{bmatrix} \tag{6}$$

$$M_{inv} = \begin{bmatrix} \frac{\sqrt{2}}{2}\sin\xi\left(k_{1\_inv}\Omega_1^2 - k_{2\_inv}\Omega_2^2 - k_{3\_inv}\Omega_3^2 + k_{4\_inv}\Omega_4^2\right) - k_{5\_inv}\Omega_5^2\sin\epsilon \\ \frac{\sqrt{2}}{2}\sin\xi\left(-k_{1\_inv}\Omega_1^2 - k_{2\_inv}\Omega_2^2 + k_{3\_inv}\Omega_3^2 + k_{4\_inv}\Omega_4^2\right) \\ \cos\xi\left(k_{1\_inv}\Omega_1^2 - k_{2\_inv}\Omega_2^2 + k_{3\_inv}\Omega_3^2 - k_{4\_nv}\Omega_4^2\right) + k_{5\_inv}\Omega_5^2\cos\epsilon \end{bmatrix} \tag{7}$$

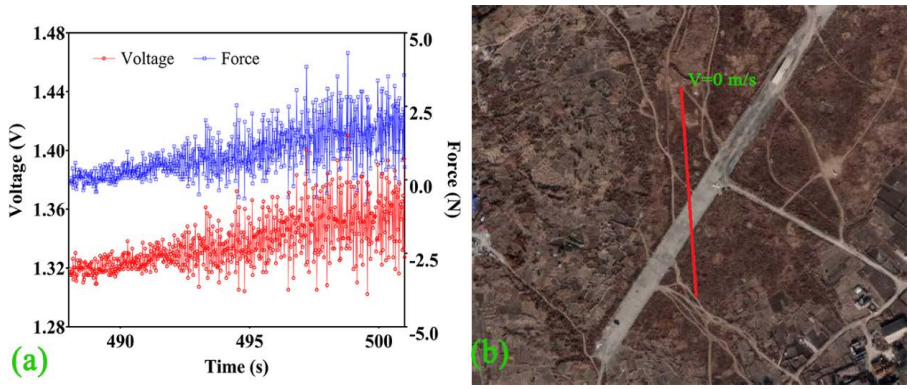

FIGURE 24. (a) Data collected by the pressure sensor and (b) the route of the unmanned carrier aircraft in flight.

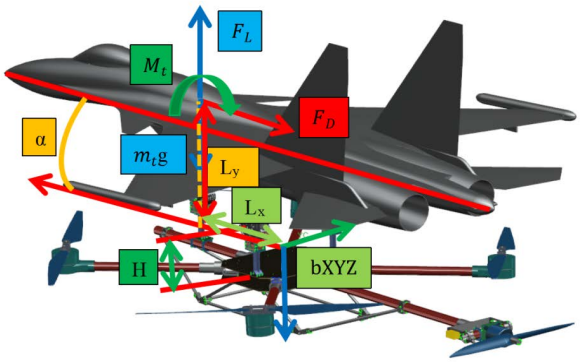

FIGURE 25. Schematic diagram of the parameters of the compound aircraft.

be seen that as the speed increases, the force acting on the connecting mechanism becomes greater with high-frequency fluctuation. The designed connecting mechanism was able to bear the unsteady force.

IV. FLIGHT TEST OF THE COMPOUND AIRCRAFT

The flight test of the compound aircraft consists of two stages. In the first stage, the unmanned carrier aircraft carries the target aircraft to achieve vertical take-off and then hovers at the desired altitude. The thrust propeller is activated in the second stage to accelerate the compound aircraft.

The experimental real-time data is used to adjust the altitude and attitude, and the pressure sensor data determines the timing of releasing the target aircraft (the separation experiment will be described in the next Section). Two installation parameters (the installation height H and the installation angle α), as shown in Fig. 25, need to be determined before the flight test. The numerical analysis in Section 2 indicates that the larger installation height gives a higher lift-to-drag ratio. Thus the installation height is increased within the safety range of torque of the connecting mechanism. As for the choice of installation angle, it will be examined numerically in the following.

A. AERODYNAMIC STUDY OF THE INSTALLATION ANGLE

In order to investigate the influence of different installation angles in flight, numerical simulations are made for the various installation angles ($\alpha = 0$, 2 and 4 degrees) and flight airspeed ($2 \sim 30$ m/s). The adopted simulation method is the same as described in Section 2.3.

Given that the take-off speed of the target aircraft at zero control rudder amount is 20.6 m/s (see Fig. 14), the airspeed range within $15 \sim 30$ m/s is first considered with the altitude kept fixed at 300 m. The obtained aerodynamic data are shown in Fig. 26. It is seen from the results that as the airspeed increases, the aerodynamic forces (including lift, drag, and torque) of the target aircraft increase significantly. Moreover, the lift of the target aircraft in the same flight airspeed also increases with the installation angle. The minimum airspeed of the target aircraft for separation is 29.2 m/s when $\alpha = 0$ degree. Whereas when $\alpha = 2$ and 4 degrees, the minimum airspeed is 20.3 m/s and 16.3m/s, respectively. Thus increasing the installation angle effectively reduces the minimum speed of the target aircraft for separation and gives a larger feasible region.

Considering that the minimum take-off airspeed of the target aircraft with maximum rudder control is 10.5 m/s, the target aircraft can separate successfully as long as it leaves the aerodynamic coupling area after separation with an airspeed greater than the above value. Moreover, the design airspeed of the unmanned carrier aircraft is about 30 m/s, so the installation angle chosen to be $2 \sim 4$ degrees is more suitable.

The curves of the rotational speed of the lift propeller are also shown in Fig. 26. Since the No. 1 and No. 2 propellers are farther away from the tail thrust propeller, the aerodynamic coupling effect is smaller, so their rotational speeds are less than the No. 3 and No. 4 propellers. As the installation angle increases, the rotational speeds of the No. 3 and No. 4 propellers also increase at a given airspeed. Furthermore, the subsequent simulations were made for the airspeed of $2 \sim 30$ m/s with the installation angles $\alpha = 2$ and 4 degrees. The results are shown in Fig. 27, the

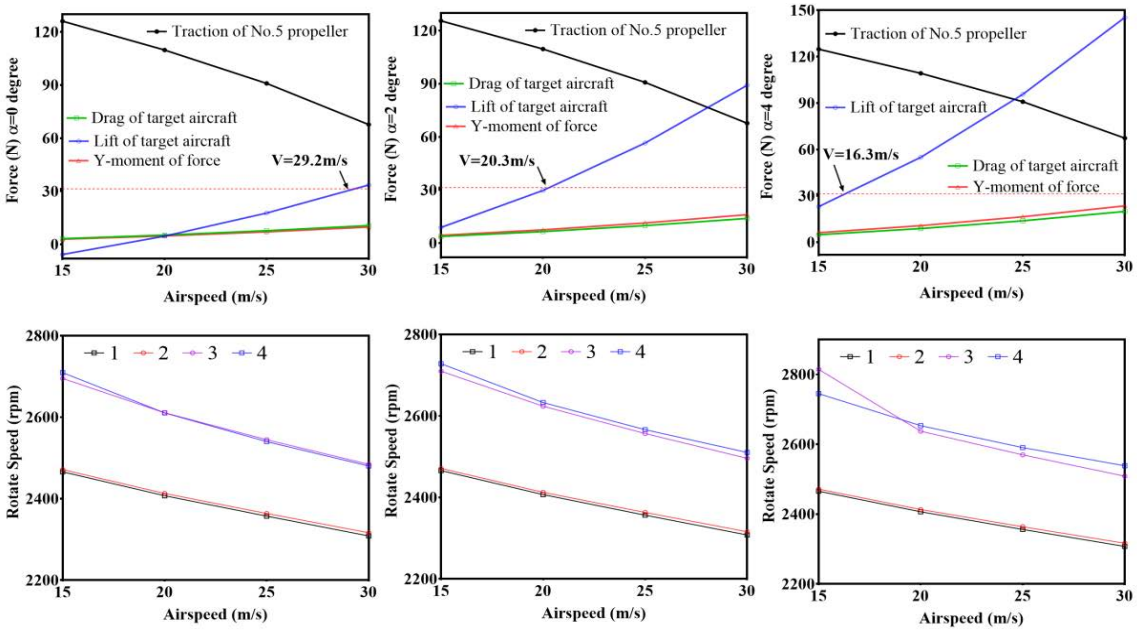

FIGURE 26. The aerodynamic forces of the target aircraft in compound flight at a fixed altitude with different installation angles (from left to right: $\alpha = 0$, 2, and 4 degrees) and the rotational speeds of the propellers.

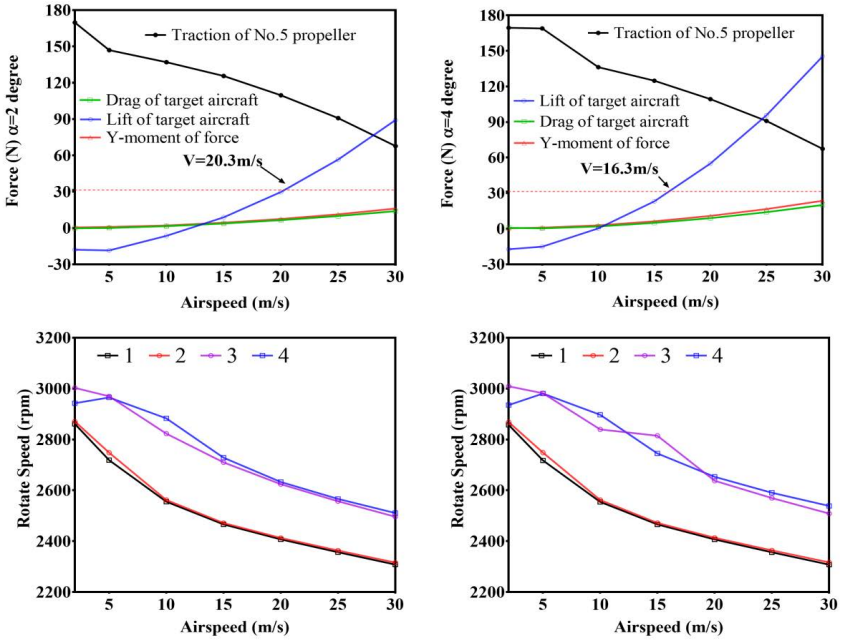

FIGURE 27. Simulation results for the airspeed of 2 ∼ 30 m/s with the installation angles $\alpha = 2$ and 4 degrees.

rotational speeds of the lift propellers are all lower than the maximum value of 3150 rpm. However, the rotation speed of the No. 3 lift propeller fluctuates when $\alpha = 4$, which might cause instability of the aircraft. Based on the above analyses, $\alpha = 2$ degrees was set for the flight test.

B. DYNAMICS MODEL OF THE COMPOUND AIRCRAFT

The dynamic model of the carrier aircraft has been given in Section 3.4. For the dynamic model of the compound aircraft, the gravity and aerodynamic forces (drag F_L and lift F_D) of the target aircraft should be taken into account. Moreover, the addition of the target aircraft also changes the moment

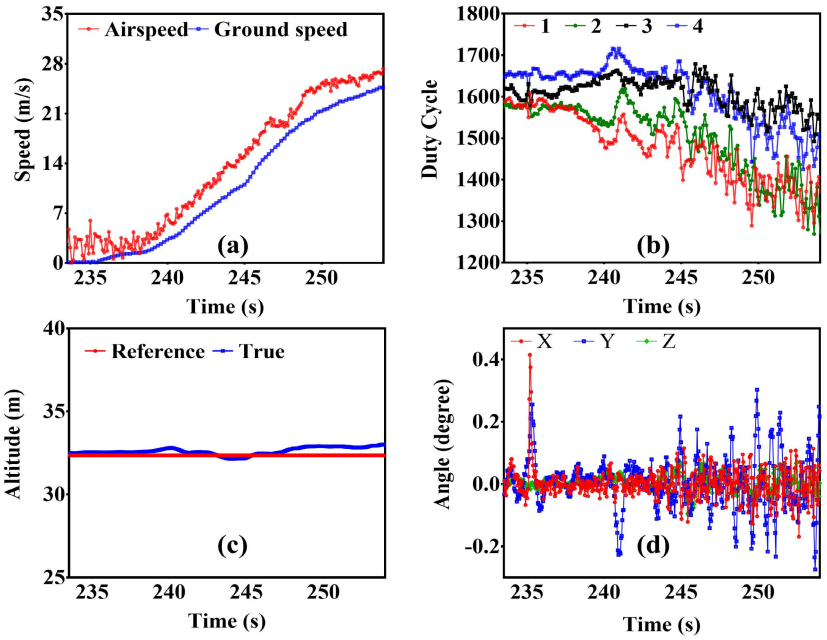

FIGURE 28. Data obtained in compound flight test. (a) Airspeed and ground speed; (b) duty cycle of four lift propellers; (c) altitude; (d) Attitude angles (X is roll angle, Y is pitch angle, Z is yaw angle).

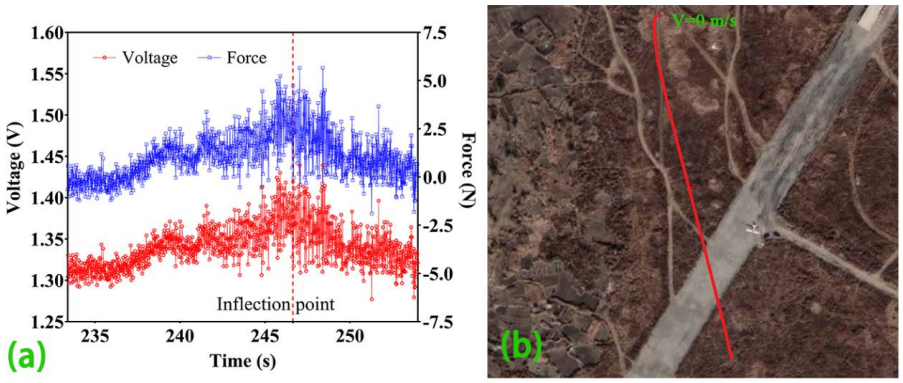

FIGURE 29. (a) Pressure sensor data and (b) flight trajectory of the compound aircraft in compound flight test.

of inertia of the compound aircraft and imposes the coupling aerodynamic force on the carrier aircraft. As a result, the mathematical model of the compound aircraft is adjusted accordingly in the following.

The total force and moment of the compound aircraft in the body coordinate system are expressed as

$$\begin{aligned} F_c &= F + F^t \\ M_c &= M + M^t, \end{aligned} \tag{8}$$

where F^t is the force of the target aircraft in the body coordinate system (9), as shown at the bottom of the next page and the moment of the target aircraft is

$$M^t = \begin{bmatrix} F_y^t L_z \\ -F_x^t L_z - F_z^t L_x + M_t \\ F_y^t L_x \end{bmatrix}, \tag{10}$$

where m_t is the mass of the target aircraft, M_t is the aerodynamic torque generated by the target aircraft, L_x and L_z are the force arm distances.

C. FLIGHT TESTS

The flight tests of the compound aircraft were carried out at a deserted airport, and the wind speed was around $2 \sim 5$ m/s during the test time. The installation angle was set to 2 degrees (± 0.5 degrees) based on the above analysis. In the flight test, the compound aircraft took off vertically and then accelerated and flew a long distance. The tests data (including the airspeed and ground speed, the duty cycle of the four lift propellers, the altitude, and the attitude) were collected by the onboard control and data acquisition system. These data, together with the pressure sensor data, are shown in Fig. 28 and Fig. 29.

FIGURE 30. Actual separation processes of four experimental separation tests.

As seen in Fig. 28 (a), the difference between the airspeed and the ground speed is within the range of $2 \sim 5$ m/s, which reflects the actual wind speed during the test time. And the duty cycle of the four lift propellers shown in Fig. 28 (b) are the same as the numerical simulation results. The altitude of the compound aircraft during flight shown in Fig. 28 (c) was in line with the reference curve, which proves the altitude control ability of the carrier aircraft. It is seen from Fig. 28 (d) that the attitude angles were subject to disturbance and fluctuated, especially the pitch angle. However, the magnitude of fluctuations was controlled within ± 0.4 degrees, which also shows the robustness of the present attitude control system and the adopted PID algorithm. The effectiveness and robustness pave the way for the successful separation test (see below).

The pressure sensor data in the compound state (see Fig. 29 (a)) is different from the data of the aircraft flying alone (see Fig. 24 (a)), and the former one first rises to a maximum value and then decays. The reason is that the aerodynamic lift of the target aircraft is less than its gravity at the beginning. The drag of the target aircraft increase with airspeed, so the force acting on the pressure sensor shows a rising trend as the airspeed increases. Meanwhile, the lift of the target aircraft also increases with airspeed and finally becomes larger than its gravity, so the force reaches a maximum value. It is obtained from Fig. 29 (a) and Fig. 24 (a) that the airspeed is around 20 m/s when the lift of the target aircraft is greater than its gravity, which is consistent with the simulation result (giving the value of 20.3 m/s).

V. EXPERIMENTAL TESTS FOR SEPARATION

As the connecting mechanism unlocks the target aircraft, the force and moment of the unmanned carrier aircraft change abruptly at the moment of separation. This sudden change is a challenge to the attitude control capability. The separation experiments were conducted to test the separation performance. The wind speed was about 2 m/s on the ground during the test time, and the compound aircraft was flying in the opposite direction of the wind. The installation angle of the compound aircraft was also chosen to be 2 degrees.

The successful and unsuccessful separation tests are described in Fig. 30. As seen in the test of Fig. 30 (a), the actual separation airspeed was 20.4 m/s, which is very close to the theoretical value of 20.3 m/s. Therefore, the lift of the target aircraft was only slightly larger than its gravity at the moment of separation. Most importantly, the power system of the target aircraft did not turn on in time, so the target aircraft dropped down and crashed. Two successful separation tests are shown in Fig. 30 (b) and (c), where the separation airspeed was 23.2 m/s and 24.8 m/s, respectively. At the separation moment, the lift of the target aircraft was much more significant due to a higher separation airspeed, and the power system of the target aircraft was activated in time. Therefore the separation process was successfully done. Although the separation airspeed in the case of Fig. 30 (c) is

$$F^t = \begin{bmatrix} F_x^t \\ F_y^t \\ F_z^t \end{bmatrix} = \begin{bmatrix} -F_D \cos\psi \cos\theta - F_L(\cos\psi \sin\theta \cos\phi + \sin\psi \sin\phi) \\ -F_D \sin\psi \cos\theta + (-F_L + m_t g)(\sin\psi \sin\theta \cos\phi - \cos\psi \sin\phi) \\ F_D \sin\theta + (-F_L + m_t g)\cos\theta \cos\phi \end{bmatrix} \tag{9}$$

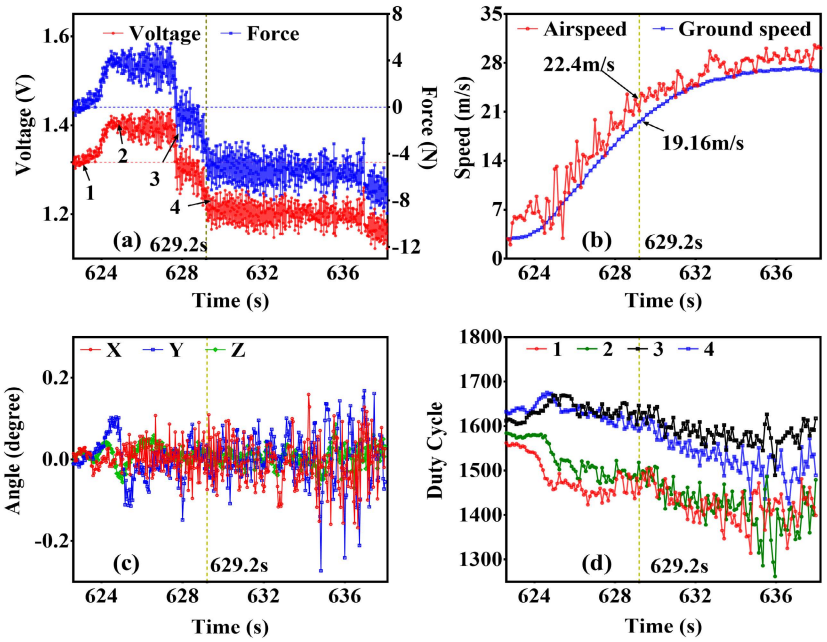

FIGURE 31. Experimental data of the unmanned carrier aircraft during the separation process. (a) Pressure sensor data; (b) airspeed and ground speed; (c) attitude of the carrier aircraft; (d) duty cycle of four lift propellers.

FIGURE 32. Actual separation process shot by (a) ground video equipment and by (b) airborne video equipment.

greater than in the case of Fig. 30 (b), the applied control rudder of the target aircraft in the former case was larger so that the target aircraft moved upward more quickly. In the failed case of Fig. 30 (d), the separation airspeed was 25.5 m/s. The reason for the failure is that the control rudder was not applied to the target aircraft, so the target aircraft flew with its head down and collided with the carrier aircraft.

The lessons learned from the above four actual separation tests show that the effective control of the target aircraft is also essential. Therefore in the subsequent six separation tests, the target aircraft was controlled to raise its head up, and the power system was opened in time. All the subsequent separation tests succeeded. The experimental data collected from one of the above tests are given in Fig. 31.

The data collected by the pressure sensor are shown in Fig. 31 (a), where point 1 is at the hovering state. The average value collected at this state is set to the initial zero value to correct the sensor drift. From point 1 to point 2, the drag of the target aircraft is larger than the lift, so the value increases with the airspeed. There are small changes in force from point 2 to point 3 on the target aircraft. From point 3 to point 4, the increase in the lift of the target aircraft is greater than the increase in drag, so the target aircraft has an upward moving trend. When the collected value is less than the initial zero value, the compound aircraft is in the pre-separation stage. Point 4 is the actual position of separation. The variation curves of airspeed, attitude, and duty cycle are given in Fig. 31 (b) (c) and (d), respectively. Fig. 31 (b) shows

that the separation airspeed of the compound aircraft is 22.4 m/s, which is great than the threshold value of 20.3 m/s. Overall, it is seen from Fig. 31 that the control system of the carrier aircraft showed the robustness of controlling the flight attitude before and after separation. The actual separation process of the target aircraft and the unmanned carrier aircraft shot by the ground video equipment and the airborne video equipment are shown in Fig. 32 (a) and (b), respectively. When the connecting mechanism unlocked the target aircraft, the applied control rudder of the target aircraft was set to maximum, which helped the target aircraft get out of the aerodynamic coupling zone quickly.

VI. CONCLUSION

A new scheme for the vertical take-off of fixed-wing aircraft has been proposed. By adopting the concept of the compound aircraft, the carrier aircraft helps the target aircraft achieve vertical take-off. The aerodynamic configuration of the present carrier aircraft has been designed and optimized. Numerical simulations and experimental tests have been done to verify the feasibility of the present scheme for vertical take-off.

The procedures of the present scheme are divided into the vertical take-off, horizontal acceleration, and separation stages. Numerical simulations were first made to evaluate the variation of aerodynamic parameters during the above stages. The obtained simulation results reflect the influences of the installation angle, installation height, and angle of attack. The aerodynamic coupling effects between the carrier and target aircraft during the horizontal acceleration and separation stages were also investigated. The lift increases with the installation angle at the same angle of attack, so the needed separation airspeed is smaller at a higher installation angle. Moreover, the concepts of lift coefficient inflection point (α_H) and maximum separation angle of attack were introduced, which are important in determining the feasible region of separation. The unsteady dynamical separation processes were also calculated using the CFD/RBD method for different angles of attack, and the case of 8° (larger than α_H) gave the successful separation.

Flight tests of the carrier aircraft and the compound aircraft were carried out to verify the present scheme, in which an unmanned aircraft with four lift and one thrust propellers was designed and manufactured to serve as the carrier aircraft. Moreover, the separation tests of the compound aircraft were also conducted. The data collected during the carrier aircraft flight demonstrate the robustness of the present control system for adjusting the altitude and attitude of the carrier aircraft. The robustness was also proved in the flight test of the compound aircraft. Moreover, several experimental separation tests were conducted, in which two failed cases show that the airspeed at the separation moment should be larger than the minimum separation airspeed and the effective control of the target aircraft is essential. After well considering the above two factors, the other separation tests all succeeded in separating the target aircraft safely. The flight tests prove the soundness of the present scheme for vertical take-off. The subsequent work will focus on designing and manufacturing a carrier aircraft with fixed-wing to get more solid information regarding the load maneuvering and aerodynamic behaviors, which will complement the present work.

ACKNOWLEDGMENT

Dong Wang and Qizhen Hong would like to thank other members of the ''Bi Fang'' Team, University of Chinese Academy of Sciences, for their valuable discussions and support.

REFERENCES

[1] J. Fozard, ''The Hawker P1127 vectored thrust fighter program-lessons learned,'' in *Proc. Space Programs Technol. Conf.*, 2012.
[2] A. Intwala and Y. Parikh, ''A review on vertical take off and landing (VTOL) vehicles,'' *Int. J. Innov. Res. Adv. Eng.*, vol. 2, no. 2, pp. 187–191, 2015.
[3] I. Maddock, M. Hirschberg, M. Hirschberg, and I. Maddock, ''The quest for stable jet borne vertical lift: ASTOVL to F-35 STOVL,'' in *Proc. AIAA Centennial Nav. Aviation Forum Years Achievements Prog.*, 2011, p. 6999.
[4] S. McGill, ''Compound aircraft transport study: Wingtip-docking compared to formation flight,'' in *Proc. 41st Aerosp. Sci. Meeting Exhib.*, Jan. 2003, p. 607.
[5] D. Wang, Q. Hong, J. Wang, H. Sun, L. Cheng, M. Li, C. Wang, X. Huang, Z. Wang, and J. Li, ''An experimental testbed for the study of visual based navigation docking of two vertical compound aircraft,'' *IEEE Access*, vol. 9, pp. 75035–75048, 2021.
[6] B. Lockett, *Flying Aircraft Carriers of the USAF: Wing Tip Coupling*. Abu Dhabi, United Arab Emirates: Lulu, 2009.
[7] P. Griesemer, J. Mueller, and M. Paluszek, ''System design of a reusable, horizontal take-off/horizontal landing two stage to orbit vehicle,'' in *Proc. 46th AIAA/ASME/SAE/ASEE Joint Propuls. Conf. Exhib.*, Jul. 2010, p. 7169.
[8] D. Zhang and Y. Zhang, ''Multidisciplinary design and optimization of an innovative nano air launch vehicle with a twin-fuselage UAV as carrier aircraft,'' *Acta Astronautica*, vol. 170, pp. 397–411, May 2020.
[9] N. Nauwynck, H. Balta, G. De Cubber, and H. Sahli, ''A proof of concept of the in-flight launch of unmanned aerial vehicles in a search and rescue scenario,'' *Acta IMEKO*, vol. 8, no. 4, pp. 13–19, 2019.
[10] P. Merlin, ''Free enterprise: Contributions of the approach and landing test (ALT) program to the development of the space shuttle orbiter,'' in *Proc. Space*, 2006, p. 7467.
[11] D. R. Harting, ''Designing the load-measuring system for the space shuttle orbiter/747 carrier aircraft approach and landing tests,'' *Exp. Techn.*, vol. 5, no. 2, pp. 1–5, Jun. 1981.
[12] A. Behrens, T. Grund, C. Ebert, R. Luckner, and J. Weiss, ''Investigation of the aerodynamic interaction between two wings in a parallel flight with close lateral proximity,'' *CEAS Aeronaut. J.*, vol. 11, no. 2, pp. 1–11, 2019.
[13] T. M. Faure, L. Hétru, and O. Montagnier, ''Aerodynamic features of a two-airfoil arrangement,'' *Exp. Fluids*, vol. 58, no. 10, pp. 1–17, Oct. 2017.
[14] B. L. Zhu, H. P. Wu, and T. H. Xiao, ''Study of aerodynamic interactions of dual flapping airfoils in tandem configurations,'' *Appl. Mech. Mater.*, vol. 160, pp. 301–306, Mar. 2012.
[15] H. Sohier, H. Piet-Lahanier, and J.-L. Farges, ''Analysis and optimization of an air-launch-to-orbit separation,'' *Acta Astronautica*, vol. 108, pp. 18–29, Mar. 2015.
[16] E. Charlton and M. Davis, ''Computational optimization of the F-35 external fuel tank for store separation,'' in *Proc. 46th AIAA Aerosp. Sci. Meeting Exhib.*, 2008, p. 376.
[17] R. F. Tomaro, F. C. Witzeman, and W. Z. Strang, ''Simulation of store separation for the F/A-18C using cobalt,'' *J. Aircr.*, vol. 37, no. 3, pp. 361–367, May 2000.
[18] K. Anandhanarayanan, K. Arora, V. Shah, R. Krishnamurthy, and D. Chakraborty, ''Separation dynamics of air-to-air missile using a grid-free Euler solver,'' *J. Aircr.*, vol. 50, no. 3, pp. 725–731, May 2013.
[19] M.-S. Liou, ''Progress towards an improved CFD method-AUSM+,'' in *Proc. 12th Comput. Fluid Dyn. Conf.*, 1995, p. 1701.

[20] R. Chen and Z. Wang, "Fast, block lower-upper symmetric Gauss–Seidel scheme for arbitrary grids," *AIAA J.*, vol. 38, no. 12, pp. 2238–2245, 2000.
[21] L. Dat Minh and C. Ha, "Modeling and control of quadrotor MAV using vision-based measurement," in *Proc. Int. Forum Strategic Technol.*, Oct. 2010, pp. 70–75.
[22] S. Bouabdallah, "Design and control of quadrotors with application to autonomous flying," Ph.D. dissertation, Ecole Polytechn. Federale de Lausanne, Lausanne, Switzerland, 2007.
[23] P. Pounds, R. Mahony, and P. Corke, "Modelling and control of a large quadrotor robot," *Control Eng. Pract.*, vol. 18, no. 7, pp. 691–699, Jul. 2010.

DONG WANG received the B.E. degree from Hebei Union University, Tangshan, China, in 2014. He is currently pursuing the Ph.D. degree with the Changchun Institute of Optics, Fine Mechanics and Physics, Chinese Academy of Sciences, China. His main research interest includes design of compound aircraft.

QIZHEN HONG received the B.E. degree from the Beijing University of Aeronautics and Astronautics, in 2017. He is currently pursuing the Ph.D. degree with the Institute of Mechanics, Chinese Academy of Sciences. His research interests include high-fidelity modeling of high-temperature flows, quantum-classical calculation for molecular collision, and design of compound aircraft.

XIN HUANG received the B.E. degree from Southwest Jiaotong University, Chengdu, China, in 2017. He is currently pursuing the M.S. degree with the Changchun Institute of Optics, Fine Mechanics and Physics, Chinese Academy of Sciences, China. His main research interests include photoelectric imaging and measurement technique.

XINBIAO PEI received the B.E. degree from Jilin University, in 2013, and the Ph.D. degree from the University of the Chinese Academy of Sciences, in 2018. His main research interests include UAV navigation and control, and multi-agent cluster control.

JING WANG is currently a Research Fellow and a Supervisor of Ph.D. candidates at the Changchun Institute of Optics, Fine Mechanics and Physics, Chinese Academy of Sciences, China. Her main research interests include optical precision instrument design and photoelectric imaging technology research.